

REPORT

TOPOLOGICAL OPTICS

Tunable topological charge vortex microlaser

Zhifeng Zhang¹, Xingdu Qiao¹, Bikashkali Midya², Kevin Liu², Jingbo Sun³, Tianwei Wu², Wenjing Liu², Ritesh Agarwal², Josep Miquel Jornet⁴, Stefano Longhi^{5,6}, Natalia M. Litchinitser³, Liang Feng^{2,1*}

The orbital angular momentum (OAM) intrinsically carried by vortex light beams holds a promise for multidimensional high-capacity data multiplexing, meeting the ever-increasing demands for information. Development of a dynamically tunable OAM light source is a critical step in the realization of OAM modulation and multiplexing. By harnessing the properties of total momentum conservation, spin-orbit interaction, and optical non-Hermitian symmetry breaking, we demonstrate an OAM-tunable vortex microlaser, providing chiral light states of variable topological charges at a single telecommunication wavelength. The scheme of the non-Hermitian-controlled chiral light emission at room temperature can be further scaled up for simultaneous multivortex emissions in a flexible manner. Our work provides a route for the development of the next generation of multidimensional OAM-spin-wavelength division multiplexing technology.

In the digital era of proliferating connections between pervasive endpoints, the tremendously growing aggregated data traffic motivates the development of innovative optical communication technologies to sustain the required massive increase in information capacity. The current information infrastructure based on wavelength and time division multiplexing—together with other degrees of freedom of light, including the amplitude, polarization, and phase—is nevertheless approaching a bottleneck. Fortunately, the full-vector nature of light provides another information dimension—namely, the angular momentum—to ease the upcoming information crunch. Whereas the spin angular momentum (SAM) associated with the circular polarization of light is limited by two states ($\sigma = \pm 1$), the orbital angular momentum (OAM)

of a vortex beam with an azimuthal phase dependence ($E \sim e^{il\varphi}$, where E is the complex electric field distribution, characterized by the topological integer $l = 0, \pm 1, \pm 2, \dots$, and φ is the azimuthal angle) (*1, 2*) creates a dimension of unlimited spatially distinguishable channels for data transmission. In addition to their potential for optical communication (*3–6*), optical vortex beams carrying OAM have also revolutionized several applications in the fields of optical manipulation (*7, 8*), imaging and microscopy (*9, 10*), and quantum information processing (*11, 12*).

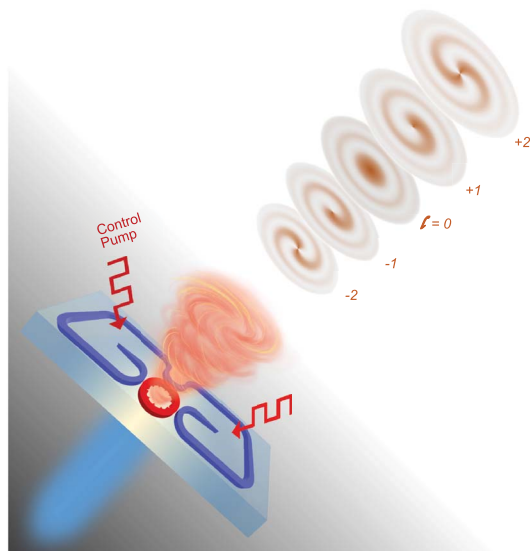
Dynamically tunable vortex light sources have become essential to bring into reality these emerging photonic technologies based on the OAM degree of freedom. Traditional bulk optical components such as spiral phase plates and forked holograms (*2, 13*)—or re-

cently developed planar optical components, including various metasurfaces (*14–17*) and silicon resonators (*18*), used for OAM beam generation—require an external input beam that originates from a separate light source. Chip-scale microlasers offer a more compact and robust solution to obtain highly pure coherent vortex modes and have been recently investigated extensively (*19–21*). However, the demonstrated miniaturized vortex lasers at telecommunication wavelengths so far lack reconfigurability, limited by their output of a predefined polarized OAM state per wavelength (*19, 20*). Nevertheless, the ongoing effort of OAM-SAM-wavelength (*3–6*) division multiplexing for multidimensional high-capacity information processing requires flexible generation and versatile manipulation of different OAM and SAM states at the same wavelength, which is not yet accessible by state-of-the-art microscale devices.

We used the transverse spin and OAM interaction to precisely maneuver the chiral light states in microring lasers. Additionally, total angular momentum conservation allows further tuning of the topological charge. The ability to simultaneously and cohesively manipulate both the SAM and OAM degrees of freedom can couple the local spin with orbital oscillation of optical cavity modes, leveraging richer functionalities in vortex light generation (*22, 23*). Spin-orbit coupling can enable effective control of the OAM handedness arising from the chiral symmetry of $\pm|l|$ wave functions, featuring the ability to flexibly generate multivortex emissions of variable $|l|$ OAMs in the full angular momentum space. Although it is straightforward to switch the chirality depending on the direction of input light in a passive microring resonator (*18*), a sophisticated active, robust strategy is required to selectively break the chiral symmetry that is intrinsically associated with a microring laser, yielding flexible control of spin-orbit interaction. Optical control of spin-orbit interaction and its induced chiral light emission have been demonstrated through spin-polarized gain generation in a semiconductor polaritonic system (*21*); however, in such a device a cryogenic environment is required, which is not suitable for practical integration in current information systems. To create a robust yet reconfigurable

Fig. 1. Schematic of non-Hermitian-controlled vortex microlaser.

The non-Hermitian interaction mediated by the externally applied control pump on the bus waveguide can flexibly be switched for the emission of OAM states with desirable chirality from the spin-orbit engineered microring.



¹Department of Electrical and Systems Engineering, University of Pennsylvania, Philadelphia, PA 19104, USA. ²Department of Materials Science and Engineering, University of Pennsylvania, Philadelphia, PA 19104, USA. ³Department of Electrical and Computer Engineering, Duke University, Durham, NC 27708, USA. ⁴Department of Electrical and Computer Engineering, Northeastern University, Boston, MA 02115, USA. ⁵Dipartimento di Fisica, Politecnico di Milano and Istituto di Fotonica e Nanotecnologie del Consiglio Nazionale delle Ricerche, Piazza L. da Vinci 32, Milano I-20133, Italy. ⁶Instituto de Fisica Interdisciplinar y Sistemas Complejos (IFISC), Consejo Superior de Investigaciones Científicas–Universidad de las Islas Baleares (CSIC–UIB), Palma de Mallorca, Spain.

*Corresponding author. Email: fenglia@seas.upenn.edu

spin-orbit coupling in an ambient-temperature environment, we developed a microlaser system in which spin-orbit interaction is controlled by an externally applied non-Hermitian coupling between the cavity modes (Fig. 1). Strategic non-Hermitian symmetry breaking facilitates the lifting of degeneracy between two spin-orbit coupled states, of which the spin is locked to the orbit direction, in a controllable manner and favors the lasing of an OAM state of desirable chirality. The spin-orbit interaction, together with the conservation of the total angular momentum, is further exploited to alter the emitted OAM state by converting the SAM into OAM, introducing additional tunability with variable topological charges at the same wavelength. This scheme can be further scaled up to simultaneously generate multiple laser vortices with an imaginary gauge (24, 25) conducted in the coupled system (26).

We considered a microring resonator supporting the two degenerate clockwise (\odot) and counterclockwise (\ominus) whispering gallery modes (WGMs) on a III-V semiconductor platform with a 200-nm-thick InGaAsP multiple quantum well layer, coupled with an additional bus waveguide of InGaAsP with two control arms, which enables the indirect coupling between the two modes (Figs. 1 and 2). By finely tuning the aspect ratio of the cross-section geometry of the waveguide, the transverse spin in the evanescent tail of guided light is engineered to be 1, which is achieved with equal amplitudes of the radial and azimuthal components of the electric field (26). The absolute value of transverse spin generated in this scheme cannot exceed 1. The spin-orbit interaction consequently couples the right-hand (\downarrow) and left-hand (\uparrow) circular polarizations with the \odot and \ominus modes, respectively, leading to spin-orbit locking for the light circulating in the microring. The degeneracy between these two countercirculating states is broken by introducing non-Hermitian mode coupling by means of the bus waveguide. By optically pumping one of the waveguide arms to create gain (generated through pumping) and loss (intrinsic material loss without pumping) contrast, an effective asymmetric coupling between the counterpropagating WGMs in the microring is obtained. The Hamiltonian of the non-Hermitian controlled microring resonator can effectively be described as

$$H_{\text{eff}} = \begin{pmatrix} \omega_{\odot} & \kappa e^{-\gamma} e^{+\gamma_L} \\ \kappa e^{-\gamma} e^{+\gamma_R} & \omega_{\ominus} \end{pmatrix} \quad (1)$$

where ω_{\odot} and ω_{\ominus} are the eigen frequencies of the two degenerate modes; κ denotes the coupling between the cavity modes without any gain or loss in the bus waveguide; $-\gamma$ describes the single pass attenuation due to the intrinsic material loss; and $+\gamma_R$ and $+\gamma_L$

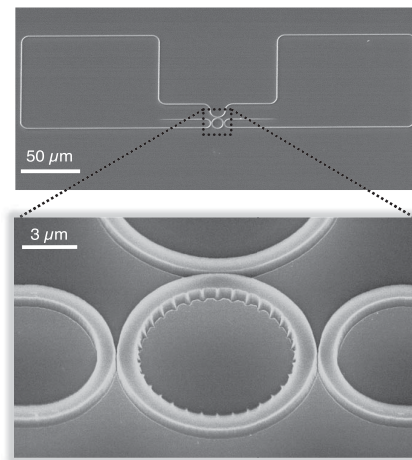


Fig. 2. Scanning electron microscope images of the tunable vortex microlaser. On an InGaAsP multiple quantum well platform, the microlaser consists of a main microring cavity coupled to an external feedback loop that enables the on-demand chiral control through selective pumping and thus enforces the unidirectional coupling between the two circulating modes in the microring. The angular grating is patterned on the inner sidewall of the microring to produce the vortex laser emission of variable topological charges.

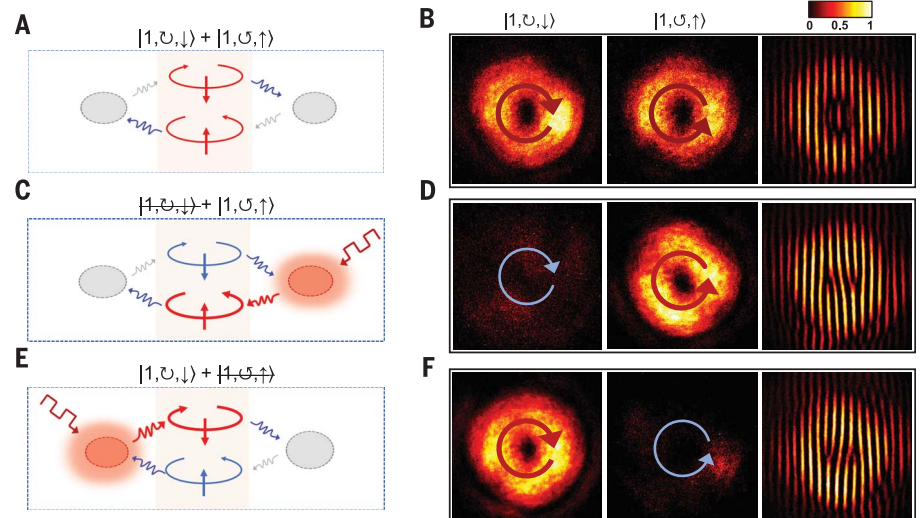


Fig. 3. Non-Hermitian chiral interactions and experimental characterization of the lasing emission. (A) In the absence of non-Hermitian interaction, both the cavity modes represented by $|l, \text{sgn}(l), \sigma\rangle$ —with $\text{sgn}(l) = \pm 1$ denoting the CCW (\ominus) and CW (\odot) oscillations, respectively, and $\sigma = \pm 1$ denoting the left (\uparrow) and right (\downarrow) circularly polarized light—are favored for lasing action. (B) Corresponding experimentally measured output emissions and off-center self-interference pattern of both the states. (C and D) Lasing emission of left-chiral mode measured after the introduction of non-Hermitian interaction applied by the right-side control pump. (E and F) Lasing emission of right-chiral mode measured after reversing the non-Hermitian interaction applied by the left-side control pump. The shaded rectangular area at left denotes the microring cavity, and the shaded elliptical areas indicate non-Hermitian control arms. The red and gray arrows outside the cavity denote the gain and loss feedback, respectively, and the blue arrows represent energy outcoupled from the cavity into the environment. Because of the unidirectional gain feedback, the red cavity mode is selectively favored for chiral lasing action, whereas the blue cavity mode is suppressed.

represent the single pass amplification from the optical pumping applied to the right and left control arms, respectively. This effective Hamiltonian can also be transformed into a parity-time symmetric-like form (27) by using the basis of $\omega_{\odot} + i\omega_{\ominus}$ and $\omega_{\odot} - i\omega_{\ominus}$ states (26). In the absence of optical pumping on the control arm ($\gamma_L = \gamma_R = 0$), the overall coupling strength between \odot and \ominus modes approaches zero because of the strong intrinsic material loss of the InGaAsP multiple quantum well ($\gamma \gg 1$) (Fig. 3A). When the left (or right) con-

control arm is selectively pumped, the intrinsic material loss on the left (or right) is then overcome by net optical gain, $\gamma_L > \gamma$ (or $\gamma_R > \gamma$). However, the unpumped right (or left) side of the waveguide remains lossy. Because of spin-orbit locking, selective pumping results in a unidirectional coupling between the \odot and \ominus modes, breaking the chiral symmetry and facilitating an effective means to controlling the chirality of the mode (Fig. 3, C and E). Under this condition, the microlaser effectively operates at an exceptional point (19).

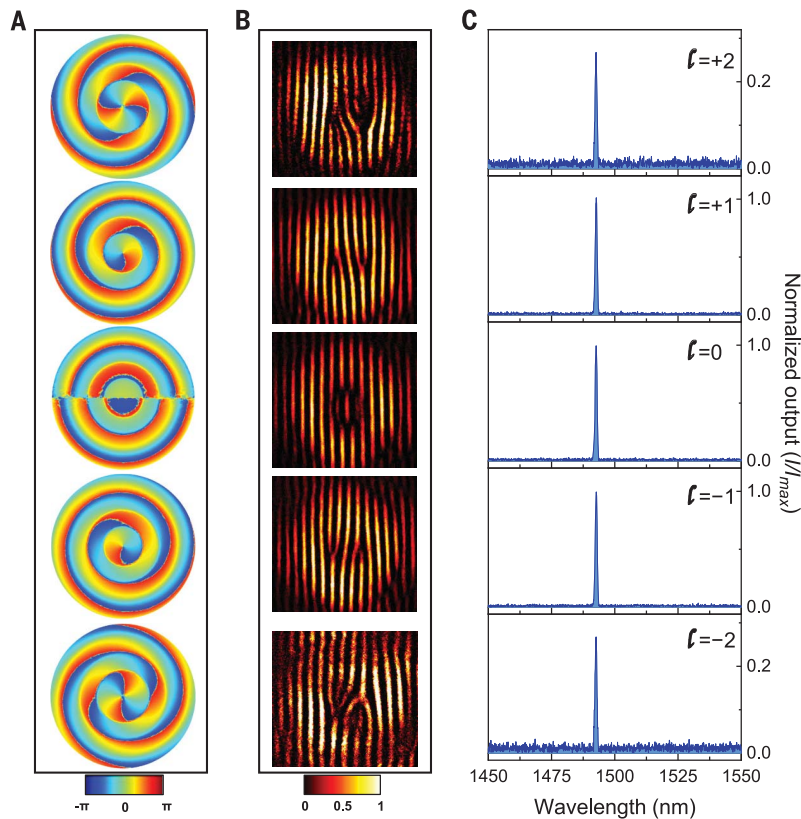


Fig. 4. Experimental characterization of different OAM states at a fixed wavelength. (A) Simulated phase distributions of OAMs of charges $l = 0, \pm 1$, and ± 2 , showing the helical phase winds 2π around the center. The OAMs of the lower three orders were achieved through spin-orbit locking, and higher-order OAMs were obtained through the spin-to-orbit coupling: $(\sigma, l) = (\pm 1, \pm 1)$ to $(\sigma, l) = (0, \pm 2)$. In both cases, the chiral symmetry was broken by controllable non-Hermitian mode coupling. (B) Corresponding experimental results showing the off-center self-interference patterns (images are enhanced for better visualization). Although no notable fringe mismatch was observed for the $l = 0$ state, a pair of inverted forks were observed for nonzero OAMs. A single fringe splits into two or three, indicating a phase wind of 2π or 4π around the center singularity point, confirming the OAM of $|l| = 1, 2$, respectively. The forks associated with opposite chirality were in opposite directions. (C) Measured lasing spectra show all five OAM lasing peaks located at 1492.6 nm, implying that the vortex microlaser can generate single-frequency vortex beams of variable OAMs simultaneously.

Unidirectional emission is robust against instabilities induced by nonlinearities above the laser threshold (28) and is essential to realize our single-frequency microlaser with reconfigurable OAM through spin-orbit coupling.

The non-Hermitian controlled microlaser was designed so that the angular momentum carried by the WGM inside the resonator is extracted into free space by introducing periodic angular scatters on the inner sidewall (Fig. 2). The angular scatters are located at $\theta_q = 2\pi q/M$ and carry a local phase of $\varphi_{\text{local},q} = 2\pi Cq(N-M)/M$, where $q \in \{0, M-1\}$; $C = \text{sgn}(\sigma)$ for the \cup and \cup modes, respectively; and N is the order of the WGM. By accounting for the rotation of local coordinates with respect to the global coordinate, the extracted global phase can be expressed as $\varphi_{\text{global},q} = 2\pi C[q(N-M) - q]/M$. Consequently, the linearly varying phase distribution creates an OAM emission with a topological charge of $l = C(N-M-1)$ and a

total angular momentum of $J = C(N-M)$. The corresponding vortex emission, containing both SAM and OAM as well as their associated chirality, can be represented as $||l|, \text{sgn}(l), \sigma$. In our experiment, the microlaser cavity has a diameter of 7 μm and a width of 0.65 μm , which supports a WGM of the order of $N = 34$ and scatter number $M = 32$ for a total angular momentum of $|J| = 2$.

To better configure the non-Hermitian-controlled chirality and its resulting spin-orbit interaction, two synchronized pump beams from a nanosecond laser were projected: one onto the microlaser cavity to carry out the lasing and the other to selectively pump one of the control arms to manipulate the chirality of the lasing (26). The chiral symmetry of the system was observed in the absence of a control pump (Fig. 3A). The emission from the resonator showed right- and left-handed circularly polarized components

of nearly balanced intensities without a net spin angular momentum (Fig. 3B). This reveals the absence of net nonzero angular momentum resulting from the coexistence of the two degenerate \cup and \cup modes. To probe the vortex nature of laser radiations, the emitted beam was split into two identical beams that were subsequently interfered with a slight offset in the horizontal direction. The acquired interferogram shows no notable fringe mismatch or discontinuity, indicating no phase winding near the center of the beam, which confirms a net-zero OAM charge (Fig. 3B). By contrast, when the control beam was switched on while illuminating only the right control arm (Fig. 3C), unidirectional laser oscillation arose in the \cup mode. The emission of nearly perfect left-handed circular polarization was consequently observed, revealing the unidirectional power circulation of the \cup mode inside the microring and spin-orbit locking. Because of phase singularity, the phase distribution changes drastically near the center of the emitted laser beam while maintaining relatively uniform distribution at outer regions. Therefore, the corresponding self-interference pattern shows a pair of inverted forks, verifying the topological charge of OAM laser emissions. In each fork, a single fringe splits into two, corresponding to an OAM charge of $+1$ (Fig. 3D). Similarly, when the control beam was only applied onto the left control arm (Fig. 3E), a nearly perfect right-handed circularly polarized emission was observed instead, demonstrating the non-Hermitian-controlled switching of chirality through spin-orbit locking. The orientations of the forks were reversed compared with the previous condition, in which the single fringe still splits into two but in the opposite direction, verifying an OAM charge of -1 (Fig. 3F).

Additional tunability of the OAM charge through the conservation of the total angular momentum in the spin-to-orbit conversion was demonstrated with the vortex microlaser by using a radial polarizer that preserves the rotational symmetry of the emitted laser beam (26). The radial polarizer allows the transmission of only radially polarized light and thus converts circularly polarized light into a linearly polarized beam in a polar coordinate. Because the radial polarizer does not break the rotational symmetry, the total angular momentum, $J = l + \sigma$, of light must remain conserved. For a given J , l can therefore be controlled through the manipulation of σ . The new OAM states with $l = \pm 2$ were achieved after the transfer of $\sigma = \pm 1$ SAMs into the demonstrated $l = \pm 1$ OAMs, respectively, when the laser beam was passed through the polarizer. The self-interference interferograms were captured to analyze the vortex reconfiguration of the emitted beams. A pair of inverted forks with three fringes were observed, revealing a

phase winding of 4π at the center, which confirmed the OAM charge $l = \pm 2$ (Fig. 4, A and B, top and bottom). Altogether, the non-Hermitian-controlled vortex microlaser is capable of producing five different OAM states ranging in $l = -2, -1, 0, +1, +2$ in a reconfigurable manner. The lasing of all these OAM states occurred at a “single” wavelength at 1492.6 nm (Fig. 4C), potentially providing five spatial channels for information modulation and communication (26). The switching time of spin-orbit coupling is in principle limited by the semiconductor optical response, with the potential to reach ultrafast OAM switching in the picosecond scale (29), so that our reconfigurable OAM microlaser, besides emitting at a fixed wavelength, is much faster than those based on thermo-optic control of WGM resonances (microsecond to millisecond time scales). Further, our non-Hermitian spin-orbit mode control scheme is scalable by applying an imaginary gauge (24, 25) to cascade sequential microrings to simultaneously generate multiple laser vortices; experimental results are given in (26).

Our tunable OAM microlaser is capable of emitting vortex beams of five different topological charges at room temperature. The non-Hermitian manipulation of chiral spin-orbit interaction offers fundamentally new functionality of controllable vortex light emission in a scalable way. The non-Hermitian control of spin-orbit interactions and thus OAM emissions is general and compatible with conventional electrical pumping schemes in which

standard p-i-n semiconductor configurations are exploited for current injection to excite optical gain (30). The toolbox of generating various vortex light at a single wavelength holds the promise for future development of multidimensional OAM-SAM-wavelength division multiplexing for high-density data transmission in classical and quantum regimes. Additionally, dynamic switching between different OAM modes in time can further increase the security of wired and wireless communication networks (26).

REFERENCES AND NOTES

1. L. Allen, M. W. Beijersbergen, R. J. C. Spreeuw, J. P. Woerdman, *Phys. Rev. A* **45**, 8185–8189 (1992).
2. A. M. Yao, M. J. Padgett, *Adv. Opt. Photonics* **3**, 161–204 (2011).
3. J. Wang *et al.*, *Nat. Photonics* **6**, 488–496 (2012).
4. N. Bozinovic *et al.*, *Science* **340**, 1545–1548 (2013).
5. I. M. Fazal *et al.*, *Opt. Lett.* **37**, 4753–4755 (2012).
6. A. E. Willner *et al.*, *Adv. Opt. Photonics* **7**, 66–106 (2015).
7. H. He, M. E. J. Friese, N. R. Heckenberg, H. Rubinsztein-Dunlop, *Phys. Rev. Lett.* **75**, 826–829 (1995).
8. M. Padgett, R. Bowman, *Nat. Photonics* **5**, 343–348 (2011).
9. L. Torner, J. Torres, S. Carrasco, *Opt. Express* **13**, 873–881 (2005).
10. C. Maurer, A. Jesacher, S. Bernet, M. Ritsch-Marte, *Laser Photonics Rev.* **5**, 81–101 (2011).
11. A. Mair, A. Vaziri, G. Weihs, A. Zeilinger, *Nature* **412**, 313–316 (2001).
12. J. Leach *et al.*, *Science* **329**, 662–665 (2010).
13. D. Naidoo *et al.*, *Nat. Photonics* **10**, 327–332 (2016).
14. N. Yu *et al.*, *Science* **334**, 333–337 (2011).
15. D. Lin, P. Fan, E. Hasman, M. L. Brongersma, *Science* **345**, 298–302 (2014).
16. M. I. Shalaev *et al.*, *Nano Lett.* **15**, 6261–6266 (2015).
17. C. W. Qiu, Y. Yang, *Science* **357**, 645–645 (2017).
18. X. Cai *et al.*, *Science* **338**, 363–366 (2012).
19. P. Miao *et al.*, *Science* **353**, 464–467 (2016).
20. W. E. Hayenga *et al.*, *ACS Photonics* **6**, 1895–1901 (2019).
21. N. Carlon Zambon *et al.*, *Nat. Photonics* **13**, 283–288 (2019).
22. K. Y. Bliokh, F. J. Rodríguez-Fortuño, F. Nori, A. V. Zayats, *Nat. Photonics* **9**, 796–808 (2015).
23. Z. Shao, J. Zhu, Y. Chen, Y. Zhang, S. Yu, *Nat. Commun.* **9**, 926 (2018).
24. S. Longhi, L. Feng, *APL Photon.* **3**, 060802 (2018).
25. S. Longhi, *Ann. Phys.* **530**, 1800023 (2018).
26. Materials, methods, and additional information are available as supplementary materials.
27. L. Feng, R. El-Ganainy, L. Ge, *Nat. Photonics* **11**, 752–762 (2017).
28. S. Longhi, L. Feng, *Photon. Res.* **5**, B1 (2017).
29. C. Huang *et al.*, *Science* **367**, 1018–1021 (2020).
30. J. Zhang *et al.*, *Nat. Commun.* **9**, 2652 (2018).

ACKNOWLEDGMENTS

Funding: We acknowledge the support from the National Science Foundation (NSF) (ECCS-1932803, ECCS-1846766, ECCS-1842612, OMA-1936276, CMMI-1635026, DMR-1809518, IIP-1718177, and CNS-2011411), U.S. Army Research Office (ARO) (W911NF-19-1-0249), and King Abdullah University of Science and Technology (grant OSR-2016-CRG5-2950-04). This research was partially supported by NSF through the University of Pennsylvania Materials Research Science and Engineering Center (MRSEC) (DMR-1720530). This work was carried out in part at the Singh Center for Nanotechnology, which is supported by the NSF National Nanotechnology Coordinated Infrastructure Program under grant NNCI-1542153. **Author contributions:** Z.Z. and L.F. conceived the project and conducted the design. Z.Z., B.M., T.W., K.L., J.S., N.M.L., and S.L. constructed the theoretical model and numerical simulations. X.Q., T.W., and W.L. fabricated the samples. Z.Z. and K.L. performed the measurements. Z.Z., B.M., L.F., J.S., N.M.L., S.L., R.A., and J.M.J. carried out data analyses. J.M.J. created the model for communication based on dynamically tunable OAMs. All authors contributed to manuscript preparation and discussion. **Competing interests:** The authors declare no competing interests. **Data and materials availability:** All data are available in the manuscript or the supplementary materials.

SUPPLEMENTARY MATERIALS

science.sciencemag.org/content/368/6492/760/suppl/DC1
Supplementary Text
Figs. S1 to S10
References (31–35)

15 January 2020; accepted 19 March 2020
10.1126/science.aba8996

Tunable topological charge vortex microlaser

Zhifeng Zhang, Xingdu Qiao, Bikashkali Midya, Kevin Liu, Jingbo Sun, Tianwei Wu, Wenjing Liu, Ritesh Agarwal, Josep Miquel Jornet, Stefano Longhi, Natalia M. Litchinitser and Liang Feng

Science **368** (6492), 760-763.
DOI: 10.1126/science.aba8996

Optical vortices on demand

Light has several degrees of freedom (wavelength, polarization, pulse length, and so on) that can be used to encode information. A light beam or pulse can also be structured to have the property of orbital angular momentum, becoming a vortex. Because the winding number of the vortex can be arbitrary, the channel capacity can be expanded considerably. Zhang *et al.* and Ji *et al.* developed nanophotonic-based methods for generating and electrically detecting light with arbitrary orbital angular momentum, a goal that has remained an outstanding challenge so far (see the Perspective by Ge). The nanophotonic platform provides a route for developing high-capacity optical chips.

Science, this issue p. 760, p. 763; see also p. 707

ARTICLE TOOLS

<http://science.sciencemag.org/content/368/6492/760>

SUPPLEMENTARY MATERIALS

<http://science.sciencemag.org/content/suppl/2020/05/13/368.6492.760.DC1>

RELATED CONTENT

<http://science.sciencemag.org/content/sci/368/6492/707.full>
<http://science.sciencemag.org/content/sci/368/6492/763.full>

REFERENCES

This article cites 35 articles, 8 of which you can access for free
<http://science.sciencemag.org/content/368/6492/760#BIBL>

PERMISSIONS

<http://www.sciencemag.org/help/reprints-and-permissions>

Use of this article is subject to the [Terms of Service](#)

Science (print ISSN 0036-8075; online ISSN 1095-9203) is published by the American Association for the Advancement of Science, 1200 New York Avenue NW, Washington, DC 20005. The title *Science* is a registered trademark of AAAS.

Copyright © 2020 The Authors, some rights reserved; exclusive licensee American Association for the Advancement of Science. No claim to original U.S. Government Works



Supplementary Material for **Tunable topological charge vortex microlaser**

Zhifeng Zhang, Xingdu Qiao, Bikashkali Midya, Kevin Liu, Jingbo Sun, Tianwei Wu,
Wenjing Liu, Ritesh Agarwal, Josep Miquel Jornet, Stefano Longhi,
Natalia M. Litchinitser, Liang Feng*

*Corresponding author. Email: fenglia@seas.upenn.edu

Published 15 May 2020, *Science* **368**, 760 (2020)
DOI: 10.1126/science.aba8996

This PDF file includes:

Supplementary Text
Figs. S1 to S10
References

Supplementary Text

1. Theoretical model and simulations of non-Hermitian controlled tunable chiral WGM

A microring resonator possesses degenerate clockwise (\mathcal{U}), CW, and counter clockwise (\mathcal{O}), CCW, modes that usually coexist in pairs and circulate in opposite directions. Due to chiral symmetry, the two-paired modes share identical lasing properties such as frequency, threshold and intensity. Consequently, the continuous phase information carried by the two modes cancel each other resulting in zero net OAM. It is therefore essential to create a unidirectional power flow in the microring cavity to extract the non-trivial phase information.

We realize a tunable chiral OAM microlaser by utilizing the unidirectional power flow enabled by the non-Hermitian coupling control between the WGMs (Fig. 1A). The Hamiltonian of the system in the linear regime can be described as:

$$H_{\text{eff}} = \begin{pmatrix} \omega_{\mathcal{U}} & \kappa e^{-\gamma} e^{+\gamma_L} \\ \kappa e^{-\gamma} e^{+\gamma_R} & \omega_{\mathcal{O}} \end{pmatrix}$$

where $\omega_{\mathcal{U}/\mathcal{O}}$ is the eigen frequency of the two degenerate modes, κ denotes the coupling between the cavity modes without any gain/loss, $-\gamma$ describes the single pass attenuation due to the intrinsic material loss, and $+\gamma_R(+\gamma_L)$ represents the single pass amplification from the optical pumping applied to the right (left) control arm, respectively. κ is designed to be 28 GHz through numerical simulations. Due to the high intrinsic material loss of InGaAsP multiple quantum wells ($> 300\text{cm}^{-1}$ at the working wavelength of the microlaser), single pass attenuation $-\gamma$ is calculated to be < -9 . Therefore, without external pumping (i.e. $\gamma_L = \gamma_R = 0$), the coupling between two modes is $\kappa e^{-g} < 3$ MHz which is effectively zero. Consequently, the two degenerated CW and CCW modes coexist with equal amplitudes as a standing wave (as shown in Fig. S1A). When the right side control arm is pumped, the optical gain overcomes the intrinsic material loss and introduces a net gain around 50cm^{-1} (i.e. $\kappa e^{-\gamma} e^{+\gamma_L} = 125.5$ GHz). As a result, the coupling from \mathcal{O} mode to \mathcal{U} mode (125.5 GHz) is much greater than the coupling from \mathcal{U} mode to \mathcal{O} mode (~ 0 Hz). The eigen vector of the Hamiltonian becomes $[\mathcal{U} \ \mathcal{O}]^T = [1 \ 0]^T$, predicting a unidirectional \mathcal{U} mode (Fig. S1B). In contrast, when the left side control arm is pumped, the coupling from \mathcal{O} to \mathcal{U} mode (~ 0 Hz) is much weaker than the coupling from \mathcal{U} mode to \mathcal{O} mode (125.5 GHz). In this case, the eigen vector of the Hamiltonian becomes $[\mathcal{U} \ \mathcal{O}]^T = [0 \ 1]^T$, leading to an opposite unidirectional \mathcal{O} mode (Fig. S1C). When considering laser emission above threshold, semiconductor laser rate equations for coupled WGM modes and carrier density (which include the α linewidth enhancement factor as well as self- and cross-saturation effects (28)) show that the unidirectional power flow solution is stable, i.e. self-oscillations induced by Hopf instabilities are avoided when the microlaser is operated in the non-Hermitian controlled unidirectional coupling scheme.

Interestingly, although our system is not parity-time symmetric (27), the Hamiltonian H_{eff} can be transformed into a parity-time symmetric-like form by changing the basis from $\omega_{\mathcal{U}}/\omega_{\mathcal{O}}$ to $\omega_{\mathcal{U}} + i\omega_{\mathcal{O}}$ and $\omega_{\mathcal{U}} - i\omega_{\mathcal{O}}$ states via the transformation matrix $T = \frac{1}{\sqrt{2}} \begin{pmatrix} 1 & 1 \\ i & -i \end{pmatrix}$. The resulting Hamiltonian $H_{\text{eff},2} = TH_{\text{eff}}T^{-1}$ takes the form:

$$H_{\text{eff},2} = \frac{\alpha I}{2} + \frac{1}{2} \begin{pmatrix} \theta & -i(\beta - \psi) \\ i(\beta + \psi) & -\theta \end{pmatrix},$$

where, I is the identity matrix, $\alpha = \omega_{\cup} + \omega_{\cap}$, $\beta = \omega_{\cup} - \omega_{\cap} = 0$, $\theta = \kappa e^{-\gamma} e^{+\gamma L} + \kappa e^{-\gamma} e^{+\gamma R}$ and $\psi = \kappa e^{-\gamma} e^{+\gamma L} - \kappa e^{-\gamma} e^{+\gamma R}$. The eigenvalues can be written as $\lambda_{\pm} = \frac{1}{2}(\alpha \pm \sqrt{\theta^2 + \beta^2 - \psi^2})$. When only one arm is pumped, the microlaser operates at an exceptional point, which is similar to previous work (19).

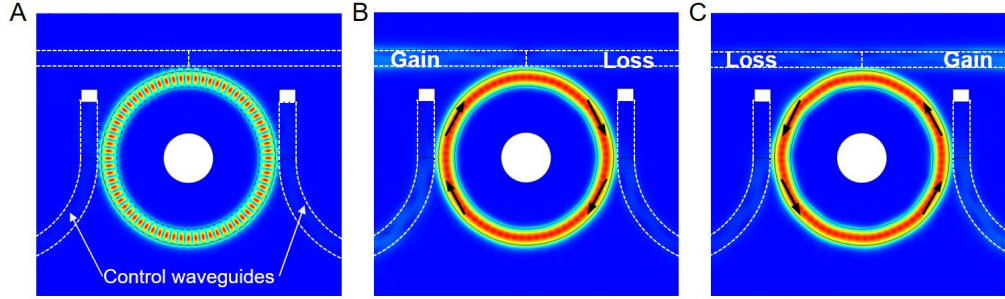


Figure S1. Full wave numerical simulation results of chiral cavity modes. (A) Electric field distribution in the microring resonator without any control pumping. Interference patterns can be seen clearly due to the coexistence of both \cup and \cap modes. (B) Electric field distribution with left-side control arm pumped, leading to unidirectional \cup mode lasing. (C) Electric field distribution with right-side control arm pumped, leading to unidirectional \cap mode lasing.

2. Transverse spin design and spin-orbit coupling of light

The transverse spin, in which the electric field rotates around the axis perpendicular to the propagation direction of light, is designed by inspecting the value of $\frac{\langle \mathbf{E} | \mathbf{L} \rangle}{|\mathbf{E}|}$, where \mathbf{E} denotes the electric field vector and \mathbf{L} denotes the unit vector of left-hand circular polarization (22, 23). From full-wave numerical simulations, we optimized the microring geometric parameters to be 200 nm in height and 650 nm in width, respectively. It is evidently demonstrated that $\frac{\langle \mathbf{E} | \mathbf{L} \rangle}{|\mathbf{E}|}$ is 0 at the inner sidewall and 1 at the outer sidewall in Fig. S2A. Therefore, the light scattered at the inner sidewall carries the same

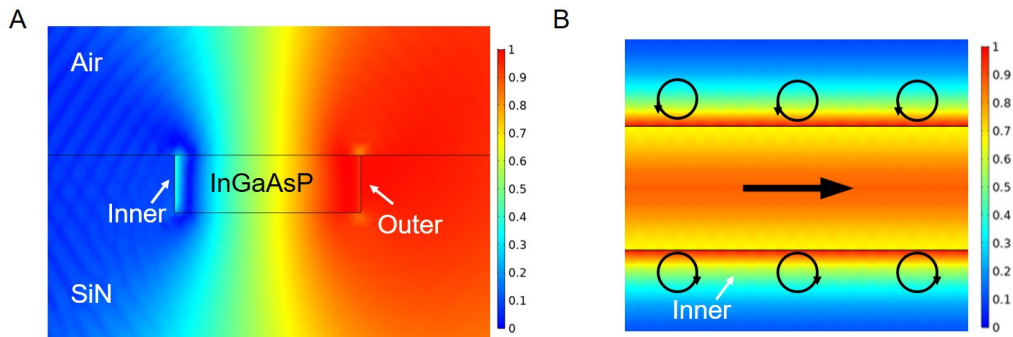


Figure S2. Design of transverse spin in the evanescent field. (A) Numerically calculated transverse spin distribution $\langle \mathbf{E} | \mathbf{L} \rangle / |\mathbf{E}|$ across the cross-section of the resonator. (B) Simulated electric field intensity distribution. The resulting local spin is locked with the orbital motion of the cavity mode. Bold black arrow denotes the powerflow direction and arrowed circles denote the local spin directions.

spin angular momentum (i.e. right circular polarization) that is locked with the corresponding orbital angular momentum of guided light (i.e. CW mode) as shown in Fig. S2B.

3. Conservation of total angular momentum and spin-to-orbit conversion

Unless rotational symmetry is broken, the total angular momentum of light remains unperturbed. Therefore, it is possible to transfer non-zero SAM into OAM to extend the tunability of the OAM generation from the microlaser. The light emitted out from the OAM microlaser carries $l = C(N - M - 1)$ and $C = \text{sgn}(\sigma)$ with a total angular momentum $J = C(N - M)$. Consequently, by transferring SAM into OAM, new OAM states characterized by $l = C(N - M)$ and $\sigma = 0$ can be generated.

In order to implement the spin-to-orbit conversion in experiments, we have designed and fabricated a rotationally symmetric metallic concentric ring polarizer as shown in Fig. S3. The periodicity Λ of the metallic rings in the radial direction was optimized to be 600 nm, which is less than half of the OAM microlaser emission wavelength. In addition, the gap size of the polarizer wire grating was optimized to be 300 nm, which is narrow enough to transmit only radially polarized light but reflect the azimuthally polarized light. Without breaking rotational symmetry, transmitted light carries zero SAM after passing through the radial polarizer. The resultant beam therefore carries an OAM charge of $C(N - M)$ as $\sigma = 0$ and $J = 0$. This result can be verified with the Jones matrices. The emitted light of the microlaser can be described as $\frac{\sqrt{2}}{2} \begin{bmatrix} 1 \\ Ci \end{bmatrix} e^{iC(N-M-1)}$, which can be decomposed into two orthogonal components $\frac{\sqrt{2}}{2} \begin{bmatrix} \cos \varphi \\ \sin \varphi \end{bmatrix} e^{iC(N-M)} + \frac{\sqrt{2}}{2} Ci \begin{bmatrix} -\sin \varphi \\ \cos \varphi \end{bmatrix} e^{iC(N-M)}$. The first (second) term represents the radially (azimuthally) polarized component with an OAM charge of $C(N - M)$. When the light illuminates upon the radial polarizer, the azimuthal component is reflected and only the radial component passes through, leading to the change in the OAM charge.

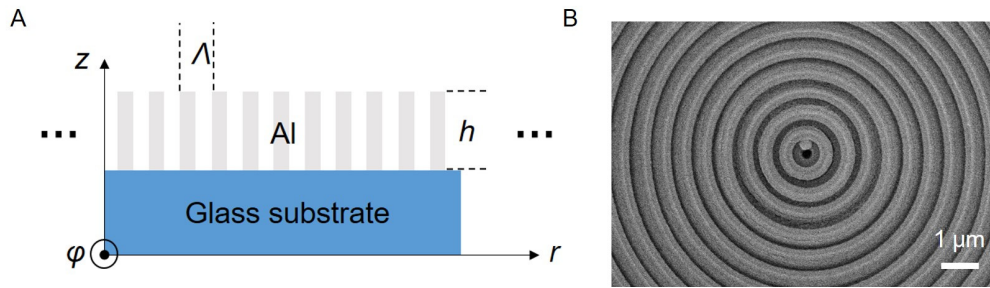


Figure S3. Radial polarizer. (A) Cross section schematic of the metallic ring radial polarizer. The periodicity Λ of the metallic rings in the radial direction is optimized to be 600 nm with duty cycle of 300 nm and h of 200 nm. (B) SEM image of the radial polarizer.

4. Fabrication of chiral laser devices and radial polarizers

The OAM microlaser was fabricated using electron-beam lithography and plasma etching techniques, following the fabrication flow shown in Fig. S4. A negative electron beam lithography resist hydrogen silsesquioxane (HSQ) in the methyl isobutyl ketone

(MIBK) solution was used for patterning. The concentration ratio of HSQ (FOX15) to MIBK was adjusted such that an adequately thick layer of resist is formed for etching after exposure and developing. The resist was then soft baked and patterned by electron beam exposure, where incident electrons made HSQ structurally amorphous. The patterned wafer was then immersed and slightly stirred in tetramethylammonium hydroxide (TMAH) solution (MFCD-26) and rinsed in deionized water for 60 seconds. The remaining HSQ served as a mask for the subsequent inductively coupled plasma dry etching process, with BCl_3 and Ar. After etching, HSQ resist was removed using buffered oxide etchant (BOE). Next, a Si_3N_4 (silicon nitride) coating was deposited by means of plasma-enhanced chemical vapor deposition (PECVD). The wafer was then bonded to a glass slide, which functions as a base. Finally, the InP substrate was removed by wet etching with a mixture of HCl and H_3PO_4 .

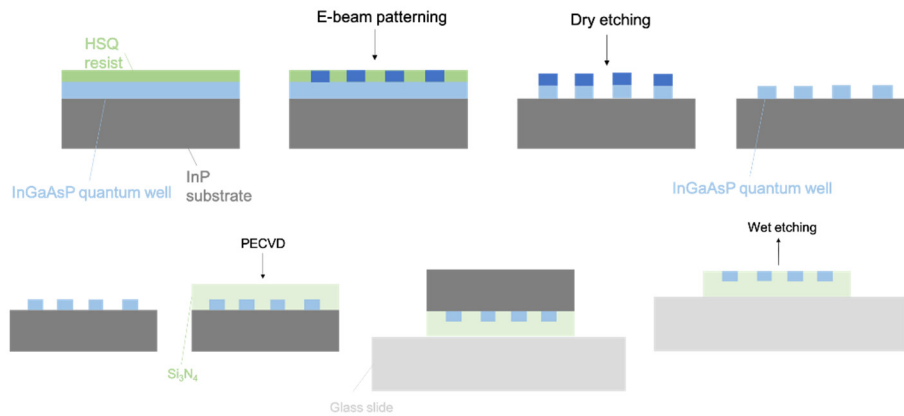


Figure S4. Fabrication flow of the OAM microlaser.

The radial polarizer was fabricated via a standard lift-off process shown in Fig. S5. ZEP-520A was used as a positive electron beam lithography resist and spin-coated onto a glass slide. After baking, a thin layer of anti-charging agent was spin coated onto the resist. The structure was then patterned by electron beam lithography, and metals (10nm Cr and 200nm Al) were deposited afterwards by physical vapor deposition (PVD). Finally, the chip was soaked in acetone for lift-off.

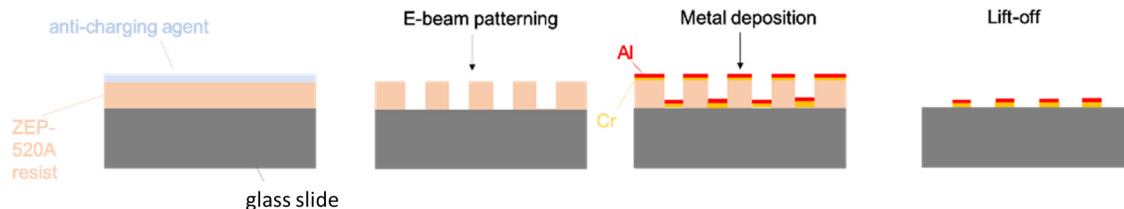


Figure S5. Fabrication flow of the radial polarizer.

5. Optical measurement of chiral single vortex emission

Figure S6 shows the measurement setup used to obtain the laser spectral characteristics and to confirm the vortex nature of the emitted radiation.

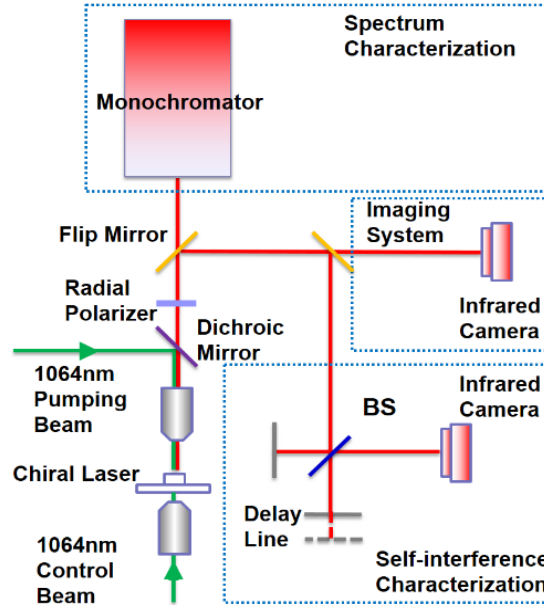


Figure S6. Optical measurement setup of the OAM microlaser.

The fabricated OAM laser was pumped on the front side by a nanosecond pulsed laser with a 50 kHz repetition rate and 8 ns pulse duration at a wavelength of 1064 nm. The pump power was controlled with a variable neutral density (ND) filter, monitored by a power meter. The pump beam was selectively reflected by a long-pass dichroic mirror (with 1180 nm cutoff wavelength) and focused onto the microring cavity using a Mitutoyo 20X near infrared (NIR) long-working distance objective (NA = 0.4). Additional control pumping beam was projected onto the control arms through a Mitutoyo 10X NIR long-working distance objective (NA = 0.28) from the backside (through the SiN substrate). The laser emission from the front side was collected by the aforementioned 20X microscope objective, passed through the radial polarizer on demand and guided into a monochromator for spectral analysis in the 1450 to 1550 nm range. The beam was also passed through combinations of quarter waveplate and linear polarizers into an imaging system for polarization characterization. Finally, the self-interference of the beam was utilized to characterize OAM nature through a Michelson interferometer. To accomplish this, the emitted beam was split into two, and recombined with an off-center, quasi-parallel beam alignment to form an interference pattern recorded by a CCD camera. Because of the nanosecond pulsed optical pumping, the lasing duration is also in the nanosecond range. In order to ensure a time overlap between the split beams, the optical path of one arm of the interferometer was adjusted with a delay line.

Measurement results of circularly polarized OAM emissions can be found in Fig. 3. After the beam transmitted through the fabricated radial polarizer, the corresponding polarization state became radial polarization, which was verified by applying a linear polarizer in the optical path and analyzing the polarization of the beam after the linear polarizer (Fig. S7). The full donut became a two-lobe pattern which rotates according to

the direction of the linear polarizer, confirming that the fabricated polarizer radially polarizes the beam effectively.

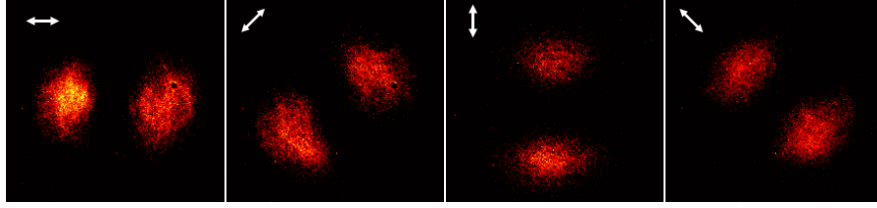


Figure S7. Polarization states after passing through the radial polarizer. White arrows represent here the direction of the linear polarizer.

The light-light curve of the vortex microlaser reveals the lasing threshold as shown in Fig. S8. The kink in the curve corresponds to the lasing threshold of the microlaser, confirming the laser action.

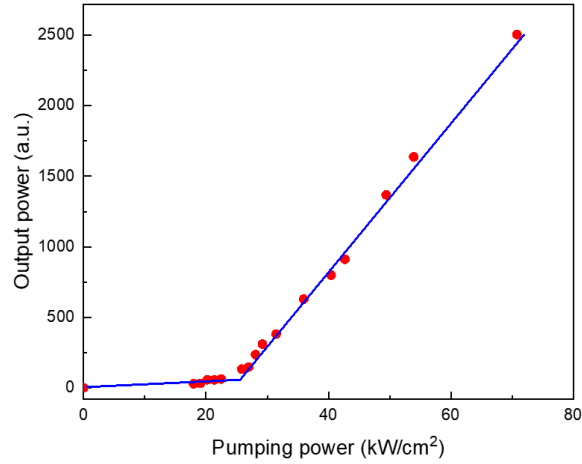


Figure S8. Light-light curve of the single OAM microlaser.

6. Highly scalable non-Hermitian-controlled multi-vortex generation based on an imaginary gauge

Here, we demonstrate that the strategy of non-Hermitian controlled single chiral vortex lasing can be generalized for multiple vortex generation in a scalable way by harnessing the concept of imaginary gauge fields (24, 25). For demonstration, we have designed and experimentally characterized integrated microring laser system capable of emitting two vortices of desirable chirality. We consider the two-microring system with two control waveguides between them shown in Fig. S9. This coupled system in the linear regime of operation is governed by the following Hamiltonian:

$$H = \begin{pmatrix} \omega_{\mathcal{U}}^L & 0 & \kappa e^{-\gamma} e^{+\gamma_B} & 0 \\ 0 & \omega_{\mathcal{U}}^L & 0 & \kappa e^{-\gamma} e^{+\gamma_T} \\ \kappa e^{-\gamma} e^{+\gamma_T} & 0 & \omega_{\mathcal{U}}^R & 0 \\ 0 & \kappa e^{-\gamma} e^{+\gamma_B} & 0 & \omega_{\mathcal{U}}^R \end{pmatrix}$$

where $\omega_{\mathcal{U}/\mathcal{U}}^{L/R}$ denotes the \mathcal{U}/\mathcal{U} resonance of WGM mode in left/right ring respectively, κ denotes the coupling of modes between two different rings without any gain or loss control, $-\gamma$ is the single-pass attenuation from the intrinsic material loss, and $+\gamma_T/+\gamma_B$ are the optical amplification from the top/bottom waveguides, respectively. An unbalanced amplification in the upper and bottom arms provides asymmetric coupling between either clock-wise or counter-clock-wise modes in the two rings, corresponding to an effective imaginary gauge field $h = \frac{\gamma_B - \gamma_T}{2}$ (25). The dual ring system is designed with the same ring/waveguide geometrical parameters as the single ring system.

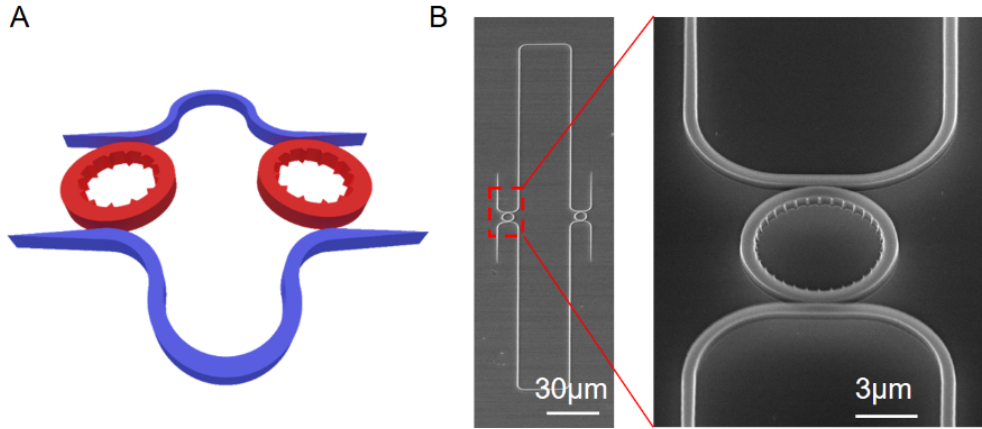


Figure S9. Schematic design and SEM pictures of a two microring OAM lasers. (A) Two microrings coupled with each other through two waveguide control arms that implement a synthetic imaginary gauge field, i.e. asymmetric mode coupling. Modes in the two rings with equal oscillation directions can couple with each other (i.e. the \mathcal{U}/\mathcal{U} modes couple with \mathcal{U}/\mathcal{U} modes, respectively). Unbalanced gain in upper and lower control waveguide arms yields asymmetric mode coupling. (B) SEM pictures of a fabricated laser system. Microring radius is $3.5 \mu\text{m}$, width is $0.65 \mu\text{m}$ and height is 200 nm . $M = 32$ periodic scatters are patterned at the inner sidewall of the microring and WGM order $N = 32$.

Without external pumping, i.e. for $\gamma_T = \gamma_B = 0$, the coupling strength of the modes between different rings is again negligible due to the high intrinsic material loss γ . As such, \mathcal{U} and \mathcal{U} modes can coexist with equal amplitude in both microring resonators, resulting in a zero net OAM charge as shown in Fig. S10A. When the upper control waveguide is pumped ($\gamma_T > 0, \gamma_B = 0$), an effective non-vanishing imaginary gauge h is realized and optical gain overcomes the intrinsic material loss and introduces a net gain around 50 cm^{-1} (i.e. $\kappa e^{-\gamma} e^{+\gamma_T} = 125.5 \text{ GHz}$). As a result, the coupling from the \mathcal{U}^L mode to the \mathcal{U}^R mode (125.5 GHz) is much greater than the back coupling ($\sim 0 \text{ Hz}$).

Simultaneously, the coupling from the \mathcal{U}^R mode to the \mathcal{U}^L mode (125.5 GHz) is much greater than the back coupling (~ 0 Hz). The eigenvector of the Hamiltonian is therefore $[\mathcal{U}^L \quad \mathcal{U}^L \quad \mathcal{U}^R \quad \mathcal{U}^R]^T = [0 \quad 1 \quad 1 \quad 0]^T$, which corresponds to unidirectional lasing of \mathcal{U}/\mathcal{V} modes in left/right ring resonators [Fig. S10B]. In contrast, when the bottom control waveguide is pumped the gauge field h is reversed, resulting in lasing with opposite chirality shown in Fig. S10C.

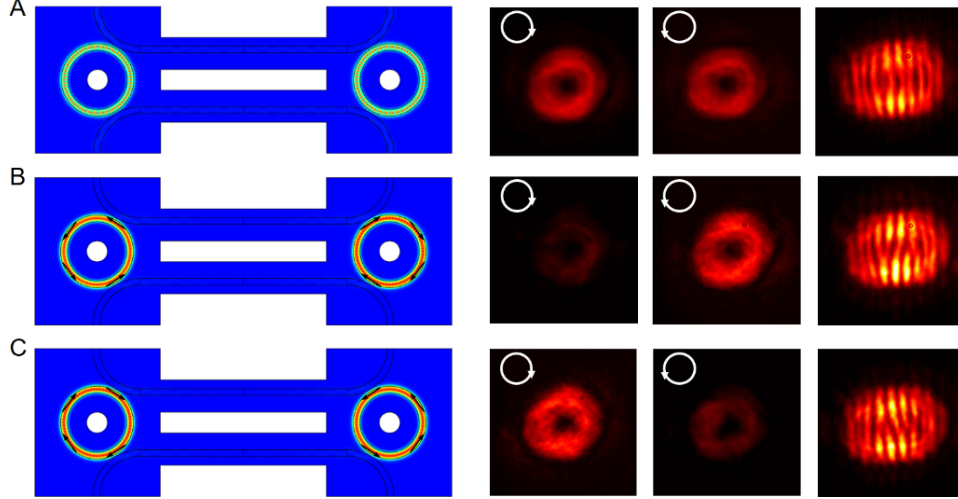


Figure S10. Characterization of chirality tuning of two OAM microlaser system. (A) None of the two control arms were pumped (i.e. $h = 0$), and emission was captured from the left-side ring laser only. The right hand circular polarized component is about equal to the left hand circular polarized component. Off-center self-interference shows no fork. (B) The upper control arm was pumped (i.e. $h < 0$) and caused lasing with \mathcal{U} mode in the left-side ring and \mathcal{V} mode in the right-side ring. The left-hand circularly polarized component was dominant in the left-side ring emission. Off-center self-interference shows a pair of forks where one fringe split into two. (C) The lower control arm was pumped (i.e. $h > 0$) and caused lasing that has opposite chirality to panel (B) behavior. The right-hand circular polarized component is dominant in the left-side ring emission. Off-center self-interference also shows a pair of forks where one fringe split into two but in the opposite direction of (B) forks.

7. Dynamically tunable OAM laser for enhanced, secure communications

There are different ways to exploit OAM in wired and wireless communications system. In the simplest form, OAM can be defined as a modulation scheme, in which different symbols are mapped to different OAM modes. For example, in a binary ($M=2$) OAM modulation, symbol or bit 0 corresponds to mode l_0 and symbol or bit 1 corresponds to an orthogonal mode l_1 . Higher order modulations, e.g., $M=4$, can similarly be defined by assigning different symbols (e.g., 00, 01, 11, 10) to different modes (l_0 to l_3 or l_{-3} , l_{-1} , l_1 , and l_3). The achievable data-rate of M-OAM modulation depends on the modulation order M and the duration of the symbol, the latter being related to the time needed for the OAM mode to be established at the transmitter and the required integration time at the receiver to recover it. Therefore, a device able to dynamically and

quickly change between modes is needed, such as the first- and one-of-a-kind tunable OAM laser reported in this work. As we discussed in the main text, the switching time in our structure is mainly determined by the carrier lifetime of the semiconductor material, which leads to very short times and, thus, potentially very high modulation bandwidths. As suggested in (6), beam splitters, OAM mode sorters or even integrated photonic circuits can be utilized to combine different OAM modes at the transmitter and, correspondingly, split them at the receiver.

Orbital angular momentum (OAM) is more commonly exploited in conjunction with other modulation schemes. At the very least, each OAM source can be modulated following on/off keying. Alternatively, different modulations (such as coherent quadrature and phase), can be applied after laser emission. Moreover, by leveraging thermal modulation to control the resonance of individual resonators coupled with the imaginary gauge (Section 6 in the Supplementary Materials), we can design our OAM source at different wavelengths and integrate them into arrays. The fact that for a given source all the OAM modes occur at the exact same wavelength enables simultaneous OAM multiplexing and WDM for high-capacity applications. Then, once again, by means of beam splitters & OAM mode sorters or integrated photonic circuits, the beams can be combined. The resulting multiplexed beam can be intended for a single user to process the aggregated information, or for a group of users who process only the information carried by a specific mode. Due to its intrinsic space-time dependent nature and many times misleadingly motivated by the way OAM is generated in lower frequency communication systems (namely, through phased antenna arrays), OAM multiplexing and Multiple-Input Multiple-Output (MIMO) communications have been often discussed together (31). While physically different, from the communication perspective they are conceptually equivalent and, thus, share the same fundamental limits (32). Increasing the number of orthogonal modes leads to a proportional increase in capacity, but not without an increasing complexity at the receiver, whose ability to separate orthogonal OAM modes ultimately bottlenecks the achievable capacity. As with any other communication technique, OAM and MIMO can also be utilized complementarily together (33). In all these cases, a tunable OAM laser is needed to support time-varying scenarios (e.g., mobile networks) that require dynamic resource allocation strategies.

Last but not least, OAM can also be leveraged to increase the security of wired and wireless communication networks. First, the strict requirements on the placement of the receiver to properly recover the OAM mode and its susceptibility to multi-path propagation would require an eavesdropper to be perfectly aligned with the transmitter and most likely blocking the receiver itself. While it has been shown (34) that even miniature metallic obstacles, which would not fully block the receiver, can be used to create a replica of the signal at an off-line direction, the OAM information would be lost. Other ways in which OAM can increase the security of communications systems is through the concept of OAM orthogonal mode hopping (35). Similar to the way in which orthogonal frequency-hopping operates, in OAM hopping, the transmitter and the receiver dynamically change their OAM mode following a pseudo-random sequence only known to them as data is being transmitted. Within each mode, the source can be on/off modulated or different modulations can be applied after emission. The resulting beam is only decipherable by a receiver that has simultaneously and accordingly changed. To

enable such secure communication scheme, a transmitter able to dynamically change its OAM mode at high speed and during transmission is needed, which is the contribution of this work.

References and Notes

1. L. Allen, M. W. Beijersbergen, R. J. C. Spreeuw, J. P. Woerdman, Orbital angular momentum of light and the transformation of Laguerre-Gaussian laser modes. *Phys. Rev. A* **45**, 8185–8189 (1992). [doi:10.1103/PhysRevA.45.8185](https://doi.org/10.1103/PhysRevA.45.8185) [Medline](#)
2. A. M. Yao, M. J. Padgett, Orbital angular momentum: Origins, behavior and applications. *Adv. Opt. Photonics* **3**, 161–204 (2011). [doi:10.1364/AOP.3.000161](https://doi.org/10.1364/AOP.3.000161)
3. J. Wang, J.-Y. Yang, I. M. Fazal, N. Ahmed, Y. Yan, H. Huang, Y. Ren, Y. Yue, S. Dolinar, M. Tur, A. E. Willner, Terabit free-space data transmission employing orbital angular momentum multiplexing. *Nat. Photonics* **6**, 488–496 (2012). [doi:10.1038/nphoton.2012.138](https://doi.org/10.1038/nphoton.2012.138)
4. N. Bozinovic, Y. Yue, Y. Ren, M. Tur, P. Kristensen, H. Huang, A. E. Willner, S. Ramachandran, Terabit-scale orbital angular momentum mode division multiplexing in fibers. *Science* **340**, 1545–1548 (2013). [doi:10.1126/science.1237861](https://doi.org/10.1126/science.1237861) [Medline](#)
5. I. M. Fazal, N. Ahmed, J. Wang, J.-Y. Yang, Y. Yan, B. Shamee, H. Huang, Y. Yue, S. Dolinar, M. Tur, A. E. Willner, 2 Tbit/s free-space data transmission on two orthogonal orbital-angular-momentum beams each carrying 25 WDM channels. *Opt. Lett.* **37**, 4753–4755 (2012). [doi:10.1364/OL.37.004753](https://doi.org/10.1364/OL.37.004753) [Medline](#)
6. A. E. Willner, H. Huang, Y. Yan, Y. Ren, N. Ahmed, G. Xie, C. Bao, L. Li, Y. Cao, Z. Zhao, J. Wang, M. P. J. Lavery, M. Tur, S. Ramachandran, A. F. Molisch, N. Ashrafi, S. Ashrafi, Optical communications using orbital angular momentum beams. *Adv. Opt. Photonics* **7**, 66–106 (2015). [doi:10.1364/AOP.7.000066](https://doi.org/10.1364/AOP.7.000066)
7. H. He, M. E. J. Friese, N. R. Heckenberg, H. Rubinsztein-Dunlop, Direct observation of transfer of angular momentum to absorptive particles from a laser beam with a phase singularity. *Phys. Rev. Lett.* **75**, 826–829 (1995). [doi:10.1103/PhysRevLett.75.826](https://doi.org/10.1103/PhysRevLett.75.826) [Medline](#)
8. M. Padgett, R. Bowman, Tweezers with a twist. *Nat. Photonics* **5**, 343–348 (2011). [doi:10.1038/nphoton.2011.81](https://doi.org/10.1038/nphoton.2011.81)
9. L. Torner, J. Torres, S. Carrasco, Digital spiral imaging. *Opt. Express* **13**, 873–881 (2005). [doi:10.1364/OPEX.13.000873](https://doi.org/10.1364/OPEX.13.000873) [Medline](#)
10. C. Maurer, A. Jesacher, S. Bernet, M. Ritsch-Marte, What spatial light modulators can do for optical microscopy. *Laser Photonics Rev.* **5**, 81–101 (2011). [doi:10.1002/lpor.200900047](https://doi.org/10.1002/lpor.200900047)
11. A. Mair, A. Vaziri, G. Weihs, A. Zeilinger, Entanglement of the orbital angular momentum states of photons. *Nature* **412**, 313–316 (2001). [doi:10.1038/35085529](https://doi.org/10.1038/35085529) [Medline](#)
12. J. Leach, B. Jack, J. Romero, A. K. Jha, A. M. Yao, S. Franke-Arnold, D. G. Ireland, R. W. Boyd, S. M. Barnett, M. J. Padgett, Quantum correlations in optical angle-orbital angular momentum variables. *Science* **329**, 662–665 (2010). [doi:10.1126/science.1190523](https://doi.org/10.1126/science.1190523) [Medline](#)
13. D. Naidoo, F. S. Roux, A. Dudley, I. Litvin, B. Piccirillo, L. Marrucci, A. Forbes, Controlled generation of higher-order Poincaré sphere beams from a laser. *Nat. Photonics* **10**, 327–332 (2016). [doi:10.1038/nphoton.2016.37](https://doi.org/10.1038/nphoton.2016.37)

14. N. Yu, P. Genevet, M. A. Kats, F. Aieta, J.-P. Tetienne, F. Capasso, Z. Gaburro, Light propagation with phase discontinuities: Generalized laws of reflection and refraction. *Science* **334**, 333–337 (2011). [doi:10.1126/science.1210713](https://doi.org/10.1126/science.1210713) [Medline](#)
15. D. Lin, P. Fan, E. Hasman, M. L. Brongersma, Dielectric gradient metasurface optical elements. *Science* **345**, 298–302 (2014). [doi:10.1126/science.1253213](https://doi.org/10.1126/science.1253213) [Medline](#)
16. M. I. Shalaev, J. Sun, A. Tsukernik, A. Pandey, K. Nikolskiy, N. M. Litchinitser, High-efficiency all-dielectric metasurfaces for ultracompact beam manipulation in transmission mode. *Nano Lett.* **15**, 6261–6266 (2015). [doi:10.1021/acs.nanolett.5b02926](https://doi.org/10.1021/acs.nanolett.5b02926) [Medline](#)
17. C. W. Qiu, Y. Yang, Vortex generation reaches a new plateau. *Science* **357**, 645–645 (2017). [doi:10.1126/science.aan6359](https://doi.org/10.1126/science.aan6359) [Medline](#)
18. X. Cai, J. Wang, M. J. Strain, B. Johnson-Morris, J. Zhu, M. Sorel, J. L. O'Brien, M. G. Thompson, S. Yu, Integrated compact optical vortex beam emitters. *Science* **338**, 363–366 (2012). [doi:10.1126/science.1226528](https://doi.org/10.1126/science.1226528) [Medline](#)
19. P. Miao, Z. Zhang, J. Sun, W. Walasik, S. Longhi, N. M. Litchinitser, L. Feng, Orbital angular momentum microlaser. *Science* **353**, 464–467 (2016). [doi:10.1126/science.aaf8533](https://doi.org/10.1126/science.aaf8533) [Medline](#)
20. W. E. Hayenga, M. Parto, J. Ren, F. O. Wu, M. P. Hokmabadi, C. Wolff, R. El-Ganainy, N. A. Mortensen, D. N. Christodoulides, M. Khajavikhan, Direct generation of tunable orbital angular momentum beams in microring lasers with broadband exceptional points. *ACS Photonics* **6**, 1895–1901 (2019). [doi:10.1021/acsphotonics.9b00779](https://doi.org/10.1021/acsphotonics.9b00779)
21. N. Carlon Zambon, P. St-Jean, M. Milićević, A. Lemaître, A. Harouri, L. Le Gratiet, O. Bleu, D. D. Solnyshkov, G. Malpuech, I. Sagnes, S. Ravets, A. Amo, J. Bloch, Optically controlling the emission chirality of microlasers. *Nat. Photonics* **13**, 283–288 (2019). [doi:10.1038/s41566-019-0380-z](https://doi.org/10.1038/s41566-019-0380-z)
22. K. Y. Bliokh, F. J. Rodríguez-Fortuño, F. Nori, A. V. Zayats, Spin–orbit interactions of light. *Nat. Photonics* **9**, 796–808 (2015). [doi:10.1038/nphoton.2015.201](https://doi.org/10.1038/nphoton.2015.201)
23. Z. Shao, J. Zhu, Y. Chen, Y. Zhang, S. Yu, Spin-orbit interaction of light induced by transverse spin angular momentum engineering. *Nat. Commun.* **9**, 926 (2018). [doi:10.1038/s41467-018-03237-5](https://doi.org/10.1038/s41467-018-03237-5) [Medline](#)
24. S. Longhi, L. Feng, Mitigation of dynamical instabilities in laser arrays via non-Hermitian coupling. *APL Photon.* **3**, 060802 (2018). [doi:10.1063/1.5028453](https://doi.org/10.1063/1.5028453)
25. S. Longhi, Non-hermitian gauged topological laser arrays. *Ann. Phys.* **530**, 1800023 (2018). [doi:10.1002/andp.201800023](https://doi.org/10.1002/andp.201800023)
26. Materials, methods, and additional information are available as supplementary materials.
27. L. Feng, R. El-Ganainy, L. Ge, Non-Hermitian photonics based on parity–time symmetry. *Nat. Photonics* **11**, 752–762 (2017). [doi:10.1038/s41566-017-0031-1](https://doi.org/10.1038/s41566-017-0031-1)
28. S. Longhi, L. Feng, Unidirectional lasing in semiconductor microring lasers at an exceptional point. *Photon. Res.* **5**, B1 (2017). [doi:10.1364/PRJ.5.0000B1](https://doi.org/10.1364/PRJ.5.0000B1)

29. C. Huang, C. Zhang, S. Xiao, Y. Wang, Y. Fan, Y. Liu, N. Zhang, G. Qu, H. Ji, J. Han, L. Ge, Y. Kivshar, Q. Song, Ultrafast control of vortex microlasers. *Science* **367**, 1018–1021 (2020). [doi:10.1126/science.aba4597](https://doi.org/10.1126/science.aba4597) [Medline](#)
30. J. Zhang, C. Sun, B. Xiong, J. Wang, Z. Hao, L. Wang, Y. Han, H. Li, Y. Luo, Y. Xiao, C. Yu, T. Tanemura, Y. Nakano, S. Li, X. Cai, S. Yu, An InP-based vortex beam emitter with monolithically integrated laser. *Nat. Commun.* **9**, 2652 (2018). [doi:10.1038/s41467-018-05170-z](https://doi.org/10.1038/s41467-018-05170-z) [Medline](#)
31. O. Edfors, A. J. Johansson, Is orbital angular momentum (OAM) based radio communication an unexploited area? *IEEE Trans. Antenn. Propag.* **60**, 1126–1131 (2011). [doi:10.1109/TAP.2011.2173142](https://doi.org/10.1109/TAP.2011.2173142)
32. M. Andersson, E. Berglind, G. Björk, Orbital angular momentum modes do not increase the channel capacity in communication links. *New J. Phys.* **17**, 043040 (2015). [doi:10.1088/1367-2630/17/4/043040](https://doi.org/10.1088/1367-2630/17/4/043040)
33. Z. Zhang, S. Zheng, Y. Chen, X. Jin, H. Chi, X. Zhang, The capacity gain of orbital angular momentum based multiple-input-multiple-output system. *Sci. Rep.* **6**, 25418 (2016). [doi:10.1038/srep25418](https://doi.org/10.1038/srep25418) [Medline](#)
34. J. Ma, R. Shrestha, J. Adelberg, C.-Y. Yeh, Z. Hossain, E. Knightly, J. M. Jornet, D. M. Mittleman, Security and eavesdropping in terahertz wireless links. *Nature* **563**, 89–93 (2018). [doi:10.1038/s41586-018-0609-x](https://doi.org/10.1038/s41586-018-0609-x) [Medline](#)
35. L. Liang, W. Cheng, W. Zhang, H. Zhang, Mode hopping for anti-jamming in radio vortex wireless communications. *IEEE Trans. Vehicular Technol.* **67**, 7018–7032 (2018). [doi:10.1109/TVT.2018.2825539](https://doi.org/10.1109/TVT.2018.2825539)